JGR Space Physics

RESEARCH ARTICLE
10.1029/2020JA027935

Observational Validation of Cutoff Models as Boundaries of Solar Proton Event Impact Area

Erkka Heino[1,2] and **Noora Partamies**[1,3]

[1]Department of Arctic Geophysics, The University Centre in Svalbard, Longyearbyen, Norway, [2]Department of Physics and Technology, University of Tromsø—The Arctic University of Norway, Tromsø, Norway, [3]Birkeland Centre for Space Science, Bergen, Norway

Key Points:
- Two cutoff latitude models were tested using riometer observations and the DRAP model during 73 SPEs
- The SPE impact area is overestimatedapproximately 90% of the time in climate models
- The Dmitriev et al. (2010)cutoff model is more suited for implementation into climate models

Correspondence to:
E. Heino,
erkkah@unis.no

Citation:
Heino, E., & Partamies, N. (2020). Observational validation of cutoff models as boundaries of solar proton event impact area. *Journal of Geophysical Research: Space Physics*, *125*, e2020JA027935. https://doi.org/10.1029/2020JA027935

Received 20 FEB 2020
Accepted 24 MAY 2020
Accepted article online 20 JUN 2020

Abstract High energy protons accelerated during solar proton events (SPEs) can access the Earth's middle atmosphere at high and middle latitudes causing large-scale ionization and chemical changes. In this study, we have compared the performance of two cutoff latitude models that predict the limit of the SPE impact area in the atmosphere during 73 SPEs from 1997 to 2010. We use observations from 13 riometer stations and the *D* Region Absorption Prediction (DRAP) model to test the performance of the two cutoff latitude models by Dmitriev et al. (2010, https://doi.org/10.1029/2010JA015380) and Nesse Tyssøy and Stadsnes (2015, https://doi.org/10.1002/2014JA020508). We find similar performance from the two cutoff latitude models with respect to observations, but the Dmitriev et al. (2010, https://doi.org/10.1029/2010JA015380) model performs slightly better when observations are contrasted with the DRAP model results. The better performing model is also continuous with magnetic local time and particle energy, making it more suited for future use in climate model proton forcing. SPE forcing is currently included in climate models with a single static cutoff latitude limit at 60° geomagnetic latitude. In reality, the area that the solar protons can access is not static but varies with particle rigidity and geomagnetic conditions. We estimate that the SPE impact area is overestimated 90% of the time by this single static cutoff limit and the average overestimation of the impact area is about 15–25% for protons with energies <32 MeV.

1. Introduction

Protons and heavier ions are accelerated during solar proton events (SPEs) to high energies by solar flares and coronal mass ejection-driven-shocks (e.g., Reames, 1999; Vainio et al., 2009). These solar energetic particles,mostly protons, have energies from 10 keV/nucl to multiple GeV/nucl (Kallenrode, 2003). Due to their high energies, the particles can penetrate the Earth's closed magnetic field lines and access the Earth's atmosphere at high and middle latitudes (about >50° geomagnetic latitude). Particle access into the Earth's magnetosphere and atmosphere is controlled by the Earth's magnetic field (Størmer, 1955; Smart & Shea, 2001), characteristics of the interplanetary magnetic field (IMF), and the pitch angle distribution of the particles (Blake et al., 2001). The access of the particles from the interplanetary medium into the Earth's magnetosphere is limited in latitude by the particles' rigidity, which depends on the kinetic energy and rest mass of the singly charged particle. The lowest latitude at which a particle of a certain rigidity can reach the Earth's surface is defined as the cutoff latitude for that rigidity (Kress et al., 2010).

Since the concept of cutoff latitudes was introduced by Størmer (1955), it has been the subject of multiple theoretical and experimental studies (for a review, see Birch et al., 2005; Dmitriev et al., 2010; Smart & Sheacite, 2009). Models of cutoff latitudes are typically constructed by either tracing particle trajectories in a modeled magnetosphere to determine their cutoff latitudes (e.g., Kress et al., 2010; Smart & Shea, 2003) or by observing cutoff latitudes with polar orbiting satellites (e.g., Birch et al., 2005; Dmitriev et al., 2010; Neal et al., 2013; Nesse Tyssøy & Stadsnes, 2015). The results are then formulated into a parametrization for the cutoff latitudes with different input parameters, such as geomagnetic indices.

Ionization due to SPEs causes production of odd hydrogen (HO_x) and odd nitrogen (NO_x) species in the middle atmosphere leading to ozone (O_3) loss which can change the radiative balance of the middle atmosphere. Changes in the radiative balance of the middle atmosphere can alter the meridional temperature gradients, dynamics, and the vertical energy transfer of the lower and middle atmosphere in the polar regions (e.g., Gray et al., 2010; Sinnhuber et al., 2012). As changes in the stratospheric ozone concentration have been

shown to affect ground-level climate variability (Gillett & Thompson, 2003), a ground-level coupling effect has been suggested for energetic particle precipitation (EPP) based on model and observational results (Baumgaertner et al., 2011; Seppälä et al., 2009). Due to this coupling, an accurate implementation of EPP in climate models is necessary to understand the role of EPP in natural climate variability in longer timescales (Andersson et al., 2014; Matthes et al., 2017).

SPEs are routinely included in climate models as spatially uniform proton precipitation events poleward of 60° geomagnetic latitude (e.g., Jackman et al., 2009; Matthes et al., 2017). In reality, cutoff latitudes are dynamic and move with changing solar wind and geomagnetic conditions (e.g., Birch et al., 2005; Clilverd et al., 2007; Dmitriev et al., 2010; Leske et al., 2001; Neal et al., 2013; Nesse Tyssøy et al., 2013; Nesse Tyssøy & Stadsnes, 2015; Rodger et al., 2006). Moreover, cutoff latitudes are not uniform in magnetic local time (MLT) but display strong day-night asymmetries at middle to high geomagnetic latitudes (>50°) (Dmitriev et al., 2010; Fanselow & Stone, 1972; Neal et al., 2013; Nesse Tyssøy et al., 2013). A single static cutoff for all proton energies leads to a large overestimation of SPE energy deposition into the polar atmosphere (Heino et al., 2019; Nesse Tyssøy et al., 2013). This overestimation is greater on the dayside where cutoff latitudes reside poleward of the nightside cutoff latitudes (Dmitriev et al., 2010; Nesse Tyssøy et al., 2013; Nesse Tyssøy & Stadsnes, 2015) and particularly severe during shock periods (Neal et al., 2013; Nesse Tyssøy et al., 2013).

In this paper, we use riometer observations and a modified version of the *D* Region Absorption Prediction (DRAP) model to test two cutoff latitude models during 73 SPEs. We also discuss the implementation of proton cutoff latitudes into proton forcing for climate models.

The cutoff latitude models by Dmitriev et al. (2010) and Nesse Tyssøy and Stadsnes (2015) were chosen for this study, as they take into account the day-night asymmetry of proton cutoff latitudes and include parametrizations for <20 MeV protons. The inclusion of protons at these energies is important because they deposit most of their energy in the mid and upper mesosphere (Turunen et al., 2009) contributing to the chemical changes in that height region. Protons at these energies also have stronger day-night asymmetries than those at higher energies.

2. Observational Data

The observational data used in this study cover 73 SPEs from 1997 to 2010, listed in Table A1. SPEs are defined as time periods where the ≥10 MeV integral proton flux, measured by a geosynchronous satellite, is greater than or equal to 10 pfu (particle flux unit, $cm^{-2}s^{-1}sr^{-1}$). The occurrence times of the SPEs are taken from the National Oceanic and Atmospheric Administration's (NOAA) list of SPEs, which is available at ftp://ftp.swpc.noaa.gov/pub/indices/SPE.txt. The data set consists of 42 S1-class (maximum ≥10 MeV integral proton flux ≥10 pfu), 19 S2-class (≥100 pfu), 7 S3-class (≥1,000 pfu), and 5 S4-class (≥10,000 pfu) SPEs.

Geostationary proton flux measurements are from the Space Environment Monitor (SEM) instrument package of three different NOAA Geostationary Operational Environmental Satellite system (GOES) satellites. GOES-8 data were used for years 1997 to 2002, GOES-10 data for years 2003 to 2009, and GOES-11 data for 2010. The GOES proton flux data have a 5-min time resolution with integral channels above threshold energies of 1, 5, 10, 30, 50, 60, and 100 MeV. The integral fluxes were interpolated to needed threshold energies by fitting a power law function to the integral flux measurements at each time step.

The increased ionization in the *D* region from SPEs leads to cosmic noise absorption (CNA). Riometers (Little & Leinbach, 1958; 1959) measure cosmic radio noise continuously, typically at 30 to 40 MHz operating frequencies. CNA is determined by comparing the measured radio noise to a quiet day curve (QDC), which is the expected level of cosmic radio noise without absorption. The level of CNA is dependent on electron density and the effective electron collision frequency (e.g., Stauning, 1996). As negative charge in the *D* region is transferred from free electrons to neutrals to form negative ions in dark conditions (e.g., Verronen, Ulich, et al., 2006), the level of CNA has a strong dependence on solar illumination and is higher in sunlit conditions than in dark conditions for the same flux of precipitating particles.

Two chains of riometers are used in this study, one in northern Europe and one in northern Canada. The locations of the riometers are shown in Figure 1 and their corrected geomagnetic latitudes (CGM),

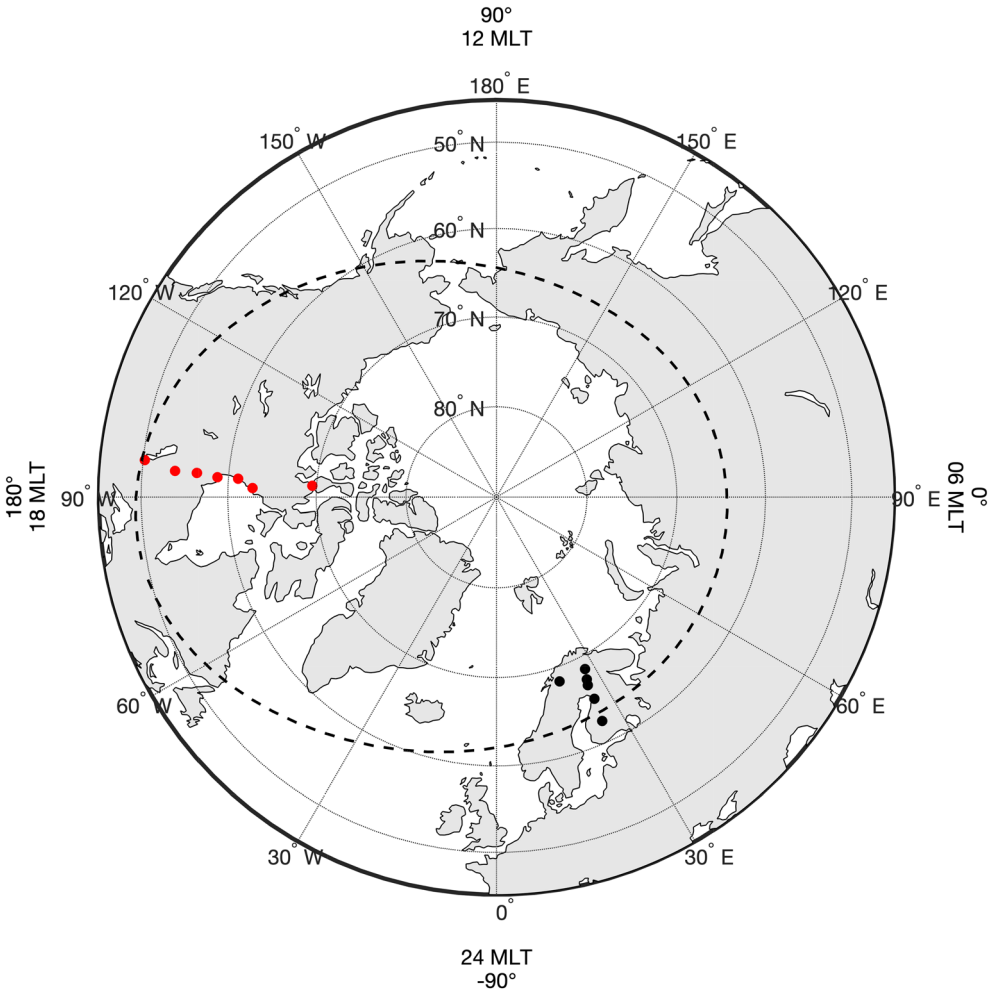

Figure 1. Geographical locations of the riometers used in the study. The GO-Canada chain riometers are marked with red dots and the Sodankylä Geophysical Observatory riometers with black dots; 60° geomagnetic latitude is marked with a black dashed line. Magnetic local times and corresponding rotated magnetic local times in degrees (*rMLT*) are shown outside the map.

invariant latitudes, and operating frequencies are listed in Table 1. The riometers in northern Europe are six of the wide-beam riometers maintained and operated by the Sodankylä Geophysical Observatory (SGO). The riometer chain in northern Canada is the Churchill line of the GO-Canada (formerly NORSTAR) wide-beam riometer array (Rostoker et al., 1995).

The SGO and GO-Canada wide-beam riometers are La Jolla analog receivers with a dual half-wavelength dipole antenna which produces a 60° beam pointing at the local zenith. The QDCs of the SGO riometers are determined using an automated method that fits a sinusoidal curve to data from the ten previous days to calculate the QDC for the current day. The baselining method of the GO-Canada riometers is based on the characterization of the shape of the quiet time cosmic radio noise rather than fitting a curve to data from the previous days. The GO-Canada baselining method is described in detail at https://aurora.phys.ucalgary.ca/norstar/rio/doc/CANOPUS_Riometer_Baselining.pdf. Time resolution of the SGO data is 1 min, and that of the GO-Canada data is 5 s. The number of available riometer stations varies from event to event.

All riometer data were averaged to 5-min time resolution, manually checked, and times with abrupt level changes, QDC problems, and clear radio interference were removed. During winter months of 2000 to 2003 (a total of 28 events), SGO data were disturbed by recurring daily radio interference. The radio interference could be either due to man-made radio frequency interference affecting the northern European

Table 1
Names, Geomagnetic Latitudes, Invariant Latitudes, and Operating Frequencies of the Riometers Used in This Study

Station name and code	Geomagnetic latitude	Invariant latitude	Frequency (MHz)
European chain:			
Abisko (ABI)	65.39°	65.00°	30.0
Ivalo (IVA)	65.13°	64.76°	29.9
Sodankylä (SOD)	64.02°	63.72°	30.0
Rovaniemi (ROV)	63.39°	62.84°	32.4
Oulu (OUL)	61.65°	61.17°	30.0
Jyväskylä (JYV)	58.92°	58.68°	32.4
Canadian chain:			
Taloyoak (TAL)	78.66°	79.47°	30.0
Rankin Inlet (RAN)	72.59°	73.53°	30.0
Eskimo Point (ESK)	70.89°	71.75°	30.0
Fort Churchill (CHU)	68.68°	69.53°	30.0
Gillam (GIL)	66.38°	67.20°	30.0
Island Lake (ISL)	63.97°	64.74°	30.0
Pinawa (PIN)	60.29°	60.98°	30.0

Note. Geomagnetic latitudes are in CGM coordinates for the year 2003 at 120 km altitude.

chain or solar radio emission that is not evident in the Canadian chain due to the different baselining approach. SGO data from these time periods were removed from the study. Data from riometers not operating at 30 MHz were converted to 30-MHz-equivalent absorption using the $f^{-1.5}$ dependence of absorption and operating frequency (Sauer & Wilkinson, 2008). This frequency dependence was chosen as it is also used in the DRAP model. Different exponents of the frequency conversion were briefly discussed by Heino et al. (2019).

The cutoff models use geomagnetic index data (3-hr time resolution *Kp* index and 1-hr time resolution *Dst* index) and solar wind data as inputs. The solar wind data were averaged to 5-min time resolution.

3. Cutoff Latitude Models

3.1. Dmitriev et al. Model

The proton cutoff latitude model by Dmitriev et al. (2010) is based on fitting ellipses to observed cutoff latitudes that were determined from proton flux measurements from NOAA's Polar Orbiting Operational Environment Satellites (POES) during two SPEs in December 2006. The maximum >10 MeV integral proton flux in the two SPEs were 1,980 and 698 pfu. The proton cutoff latitudes in the model are parametrized by the rotated magnetic local time (*rMLT*), the geodipole tilt angle (*PS*), the *Dst* index in nT, and the *Kp* index in a decimal representation. In the decimal representation of the *Kp* index, the values are multiplied by ten, and + and − are converted to +3.33 and −3.33, respectively. For example, $Kp = 6-$ is 56.67 and $Kp = 1+$ is 13.33. *rMLT* is expressed in degrees from 0° at dawn (06 MLT) to positive 180° through noon to dusk (18 MLT), while negative degrees are through midnight to dusk (see Figure 1). The Dmitriev model gives the cutoff latitudes in invariant latitudes calculated from the International Geomagnetic Reference Field (IGRF) model L shell values, so all analyses with the model in this paper are done in invariant coordinates.

Particle rigidity for a singly charged particle expressed in MV is

$$R = \sqrt{E^2 + 2E_0E}, \tag{1}$$

where E and E_0 are the kinetic energy and rest mass of the particle, both expressed in MeV.

The optimal elliptical parameters in the model are determined with multiple linear regression. The major, *as*, and minor, *bs*, semiaxes are

$$as = \Delta as + as_q, \tag{2}$$

$$bs = \Delta bs + bs_q, \tag{3}$$

where the residual semiaxes, Δas and Δbs, that eliminate the nonlinearity of the rigidity dependence are

$$\begin{aligned}\Delta as = \; & -0.568 + (-9.74 \cdot 10^{-2} + 1.16 \cdot 10^{-2}\log R) \cdot Dst \\ & + (8.55 \cdot 10^{-2} - 7.46 \cdot 10^{-3}\log R) \cdot Kp,\end{aligned} \tag{4}$$

$$\begin{aligned}\Delta bs = \; & -0.648 + (-9.74 \cdot 10^{-2} + 1.16 \cdot 10^{-2}\log R) \cdot Dst \\ & + (7.66 \cdot 10^{-2} - 7.49 \cdot 10^{-3}\log R) \cdot Kp.\end{aligned} \tag{5}$$

The semiaxes during geomagnetically quiet times ($Kp \sim 0$ and $Dst \sim 0$) are

$$as_q = \arcsin^{1/4}\left(2.41 \cdot 10^{-2} + 6.23 \cdot 10^{-5}R - 1.26 \cdot 10^{-2}\exp(-2.19 \cdot 10^{-2}R)\right), \quad (6)$$

$$bs_q = \arcsin^{1/4}\left(2.11 \cdot 10^{-2} + 6.21 \cdot 10^{-5}R - 1.19 \cdot 10^{-2}\exp(-1.81 \cdot 10^{-2}R)\right). \quad (7)$$

The coordinates, (X_0,Y_0), of the center of the ellipse in degrees can be written as

$$\begin{aligned} X_0 &= -0.29 + 0.13\log R + (3.68 \cdot 10^{-2} - 0.544 \cdot 10^{-2}\log R) \cdot Dst \\ &\quad + (-2.94 \cdot 10^{-2} + 3.4 \cdot 10^{-3}\log R) \cdot Kp, \end{aligned} \quad (8)$$

$$\begin{aligned} Y_0 &= -9.26 + 1.53\log R + (-5.43 \cdot 10^{-2} - 0.827 \cdot 10^{-2}\log R) \cdot Dst \\ &\quad + (-6.6 \cdot 10^{-2} + 10.5 \cdot 10^{-3}\log R) \cdot Kp \\ &\quad + (-7.4 \cdot 10^{-2} + 1.12 \cdot 10^{-2}\log R) \cdot PS, \end{aligned} \quad (9)$$

where X_0 is negative duskward and Y_0 is negative tailward, and PS varies between ±34.6°. The azimuth angle of the major semiaxis from the dawn-dusk line is given by

$$\phi = -54.9 + 11.3\log R. \quad (10)$$

The invariant latitude of the cutoff is

$$\lambda = 90^\circ - \sqrt{x^2 + y^2}, \quad (11)$$

where

$$x = X_0 + as \cos r\,MLT \cos\varphi - bs \sin r\,MLT \sin\varphi, \quad (12)$$

$$y = Y_0 + as \cos r\,MLT \sin\phi + bs \sin r\,MLT \cos\phi. \quad (13)$$

Dmitriev et al. (2010) reported that cutoff latitudes for E>16 MeV protons from their model are close to those observed by Ogliore et al. (2001) during geomagnetically quiet times. Rogers and Honary (2015) showed that the implementation of the Dmitriev et al. (2010) model into DRAP improved the agreement between riometer measurements and DRAP compared to the standard DRAP model which uses a cutoff latitude model by Smart (1999) with *Kp* index dependency but no MLT dependency. The Dmitriev et al. (2010) cutoff latitude model is referred to as the *Dm model* in the rest of this article.

3.2. Nesse Tyssøy and Stadsnes Model

The proton cutoff model by Nesse Tyssøy and Stadsnes (2015) is based on multiple linear regression between observed cutoff latitudes determined from POES proton flux measurements and selected solar wind and IMF parameters. The measurements used in the model are from six moderate to strong SPEs between years 2003 and 2012 with a maximum >10 MeV integral proton flux greater than 1,000 pfu. The model produces separate parametrizations for the dayside and nightside cutoffs determined by MLT. The Nesse Tyssøy and Stadsnes model provides the cutoff latitudes in CGM coordinates at 120 km altitude, so all analyses with the model in this paper are done in CGM coordinates at 120 km altitude.

The input parameters for the dayside are the *Dst* index and the B_z component of the IMF. An additional requirement in the parametrization for the dayside cutoff latitudes is a 58° geomagnetic latitude lower boundary. For the nightside, the input parameters are the *Dst* index and the third root of the ram pressure of the solar wind, p, with a lower boundary of 56° geomagnetic latitude for the cutoff latitudes. The model provides parametrization for dayside cutoff latitudes at cutoff energies of 1, 4, 8, 16, and 32 MeV. The regression formulas of the model for the dayside cutoff latitudes are

$$\begin{aligned} \lambda(1\text{ MeV}) &= 0.090Dst + 0.02B_z + 72.0^\circ, \\ \lambda(4\text{ MeV}) &= 0.085Dst + 0.04B_z + 70.5^\circ, \\ \lambda(8\text{ MeV}) &= 0.065Dst + 0.14B_z + 68.5^\circ, \\ \lambda(16\text{ MeV}) &= 0.070Dst + 0.14B_z + 66.5^\circ, \\ \lambda(32\text{ MeV}) &= 0.055Dst + 0.10B_z + 64.5^\circ. \end{aligned} \quad (14)$$

For the nightside, the parametrization is for 4 and 16 MeV cutoff energies and the nightside the regression formulas are

$$\lambda(4\ \text{MeV}) = 0.040Dst - 3.2p^{\frac{1}{3}} + 68.5°,$$
$$\lambda(16\ \text{MeV}) = 0.035Dst - 3.0p^{\frac{1}{3}} + 67.0°. \quad (15)$$

The model does not provide cutoff latitudes for dusk and dawn but suggests using interpolation between dayside and nightside cutoff latitudes.

Nesse Tyssøy and Stadsnes (2015) tested their cutoff model by applying the model to GOES fluxes during an SPE that occurred in January 2012. The modified fluxes produced energy deposition estimates that were in good agreement with those derived from POES observations during the SPE and captured the day-night asymmetry. The cutoff model by Nesse Tyssøy and Stadsnes (2015) is referred to as the *NTS model* in the rest of this article.

4. Cosmic Noise Absorption Modeling

The integral proton energy spectrum follows a power-law spectrum during SPEs (Potemra, 1972), which leads to the following relationship between CNA in decibels (A) and integral proton flux ($J(>E_t)$):

$$A = m\sqrt{J(>E_t)}, \quad (16)$$

where m is a constant and E_t is the threshold energy of the integral proton flux in MeV. In the Potemra (1972) theoretical formulation, constant m approximates a double-integral function of the exponent of the power-law proton energy spectrum, threshold energy, the effective recombination coefficient, the electron-neutral collision frequency profile, and the profile of ionization rate per unit energy. The relationship shown in Equation 16 is used by empirical CNA models which determine suitable values for m and E_t from proton flux and CNA measurements (Rogers & Honary, 2015).

The DRAP model (Akmaev, 2010; Sauer & Wilkinson, 2008) uses this approach and has been adopted by NOAA to provide real-time CNA predictions from geostationary proton flux measurements. In DRAP, the values for m and E_t are the empirical values determined by Sellers et al. (1977) for 30 MHz CNA:

$$m_d = 0.115\ \text{dB pfu}^{1/2},\ E_{t,d} = 5.2\ \text{MeV},$$
$$m_n = 0.020\ \text{dB pfu}^{1/2},\ E_{t,n} = 2.2\ \text{MeV},$$

where subscripts d and n indicate fully developed day and night ionospheres, respectively.

The twilight transition of CNA is implemented as a linear interpolation between the day and night CNA values:

$$A = A_n(1 - Z_d) + A_d Z_d, \quad (17)$$

where Z_d is the smooth weighting function by Rogers et al. (2016). In this approach, the Gauss error function is used to avoid discontinuities at the twilight bounds:

$$Z_d(\chi) = \frac{1}{2}\left(1 - \text{erf}\left(\frac{\chi - \frac{1}{2}(\chi_u + \chi_l)}{\frac{1}{2}(\chi_u - \chi_l)}\right)\right), \quad (18)$$

where erf() is the Gauss error function, χ is the solar zenith angle, and χ_u and χ_l are the upper and lower solar zenith angle bounds of the twilight transition, respectively. The twilight transition solar zenith angle bounds were optimized by Rogers et al. (2016) separately for sunrise and sunset based on CNA measurements from nine SPEs. The separation of sunset and sunrise twilight transition bounds is necessary due to the asymmetry of the effective recombination coefficient, and therefore CNA, also known as the twilight anomaly. The used optimized twilight solar zenith angle bounds from Rogers et al. (2016) are

$$\chi_{l,r} = 73.8°, \quad \chi_{u,r} = 97.9°,$$
$$\chi_{l,s} = 82.6°, \quad \chi_{u,s} = 100.6°,$$

where subscripts r and s indicate sunrise and sunset, respectively.

Cutoff latitudes are implemented in the standard DRAP model by using the cutoff energy at the riometer location (or model grid point) as the threshold energy for the integral proton flux if it is larger than the model's energy threshold $E_{t,d}$ for the dayside ionosphere or $E_{t,n}$ for the nightside ionosphere:

$$A_i = m_i \sqrt{J(>\max(E_{t,i}, E_c))}, \tag{19}$$

where subscript i is either d or n, and E_c is the cutoff energy at the riometer location. Instead of using the cutoff energy at the riometer location, we implemented cutoff latitudes at selected cutoff energies matching the NTS model.

As the DRAP energy thresholds, $E_{t,d}$ and $E_{t,n}$, are higher than some of the cutoff energies from the cutoff latitude models, the 1 MeV cutoff is not used in the CNA modeling, and the 4 MeV cutoff is not used during daytime in the CNA modeling. Conversion from UT to MLT is done by using a single time shift for each riometer chain separately rather than using each stations' individual MLT shifts. The used time shifts are 1.85 decimal hours for the European chain and −7.01 decimal hours for the Canadian chain, which are the means of the individual stations' MLT shifts for each chain. The maximum difference between the mean MLT shifts and the MLT shifts of the individual stations are 0.24 decimal hours (at ABI, 3.6° geomagnetic longitude) for the European chain and 0.19 decimal hours (at RAN, 2.85° geomagnetic longitude) for the Canadian chain. The maximum absolute change in cutoff latitude due to the difference from the mean MLT shift of the European chain is 0.58° (NTS model, 4 MeV), while the corresponding mean change is 0.01°. The maximum absolute changes for the Canadian chain due to the difference from the mean MLT shift are less than 0.4°. Based on these values and the large field of view of the wide-beam riometers, the uncertainties caused by using a single MLT shift for each chain should be small.

5. Evaluation of the Accuracy of the Cutoff Models

The linear relationship between CNA and integral proton flux is used to evaluate the effect of different cutoff energies on observed CNA and the performance of the two cutoff models. Kavanagh et al. (2004) found that CNA is best correlated with the square root of >10 MeV integral proton flux in the sunlit ionosphere. Clilverd et al. (2007) determined that CNA is proportional to $(J(>5\text{ MeV}))^{0.75}$ in dark conditions.

Ratio between CNA and $\sqrt{J(>10\text{ MeV})}$ was calculated for dayside sunlit observations where $\chi \leq 80°$ and MLT of the riometer station is between 9 and 15. Ratio between CNA and $(J(>5\text{ MeV}))^{0.75}$ was calculated for nightside dark conditions, where $\chi \geq 100°$ and the riometer station's MLT is between 21 and 03. Periods of dusk and dawn were discarded from this comparison to remove twilight effects on CNA. The data were divided separately to "cut" and "not cut" using both cutoff models with 4, 8, 16, and 32 MeV cutoff energies. Data were labeled as being cut, if the difference between the station's latitude and the cutoff latitude is less than or equal to −0.5°, and not cut if the difference is greater than or equal to 0.5°. The ±0.5° limit was chosen based on the field of view of a 60° wide-beam riometer at 90-km altitude, which is approximately ±0.46° geomagnetic latitude. As the data are divided with a single cutoff energy for each case, the stations equatorward of the cutoff latitude are also affected by higher cutoff energies.

Median ratios of CNA and integral proton flux, A/J, in sunlit conditions with 4 and 32 MeV cutoff energies as a function of geomagnetic latitude are shown in Figure 2. The Dm model is used in the panels of the left column and the NTS model is used in the panels of the right column. The two riometer chains are plotted separately in each panel, with the European chain plotted in blue and the Canadian chain plotted in red. Not cut observations are plotted with solid lines and cut observations are plotted with dashed lines. The shaded areas indicate the data between the first and third quartile of nondivided data for the European (blue) and Canadian (red) chains. The used cutoff energy is shown in the upper right hand corner of each panel. Median ratios of CNA and integral proton flux in dark conditions as a function of geomagnetic latitude are shown in Figure 3 with the same format as Figure 2, but for 4 and 16 MeV cutoff energies.

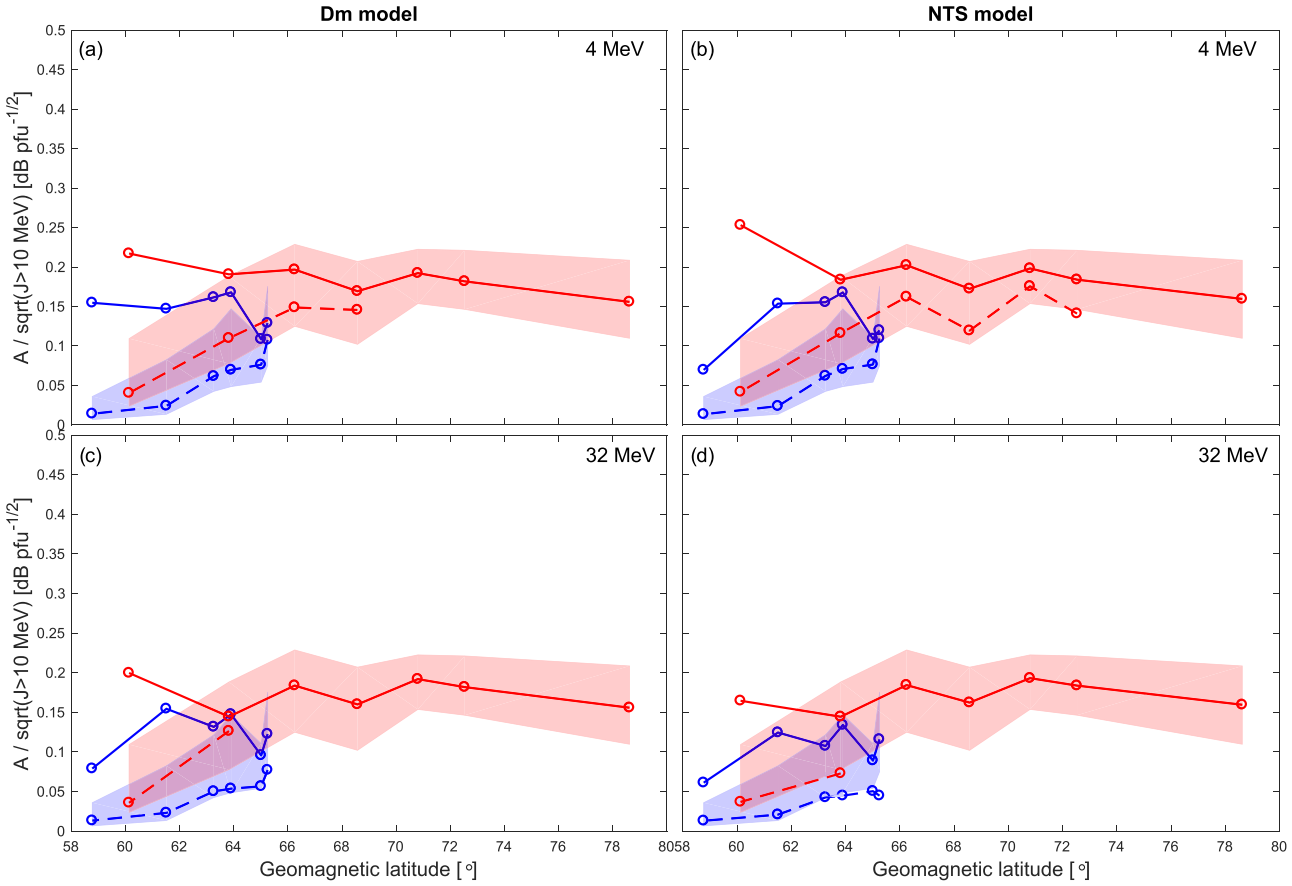

Figure 2. Median ratios of observed cosmic noise absorption and square root of >10 MeV integral proton flux as a function of geomagnetic latitude during sunlit conditions divided to cut (dashed lines) and not cut (solid lines) cases. Data in the left column are divided with the Dm model and data in the right column are divided based on NTS model. The European riometer chain is plotted in blue and the Canadian chain is plotted in red. The shaded areas indicate the data between the first and third quartiles of nondivided data for the European (blue) and Canadian (red) chains.

The not cut and cut A/J are generally higher for the Canadian riometer chain than for the European chain in sunlit conditions with all cutoff energies. The cut A/J are lower than the not cut A/J for both riometer chains and both cutoff latitude models in sunlit and dark conditions. The A/J at IVA (65.13° geomagnetic latitude) are generally low compared to adjacent stations in both sunlit and dark conditions, apart from the sunlit 32 MeV cut ratios shown in panels (c) and (d) of Figure 2. The amount of data points for calculating the cut A/J decreases with cutoff energy at the poleward stations, as the cutoff latitudes are increasingly equatorward of the stations. This leads to the smaller amount of available stations with cut observations in panels (c) and (d) of Figures 2 and 3 compared to panels (a) and (b).

The not cut A/J in sunlit conditions are fairly constant as a function of cutoff energy for both cutoff latitude models, apart from the southernmost station of both riometer chains (PIN and JYV), where the variation of not cut A/J values is large between the different cutoff energies. With 4 MeV cutoff energy, panels (a) and (b) of Figure 2, the cut sunlit A/J follow the shape of the not cut A/J well, indicating that a part of the protons responsible for CNA are cut off, but the protons at higher energies are still present causing CNA at lower altitudes. With 32 MeV cutoff energy, panels (c) and (d) of Figure 2, the cut sunlit A/J are more constant than with 4 MeV across the whole geomagnetic latitude range, as most protons responsible for CNA are cut off. Cut and not cut A/J in sunlit conditions with 8 and 16 MeV cutoff energies (not shown) combine the features seen with 4 and 32 MeV. The cut A/J values with 32 MeV cutoff energy are very close to the first quartile of nondivided data for both chains apart from the second southernmost station (ISL, 63.97° geomagnetic latitude) in the Canadian chain in panel (c) of Figure 2. This high value at ISL with 32 MeV cutoff energy is likely due to the small amount of cut data points (113) at this station, as the cut A/J values at ISL for both

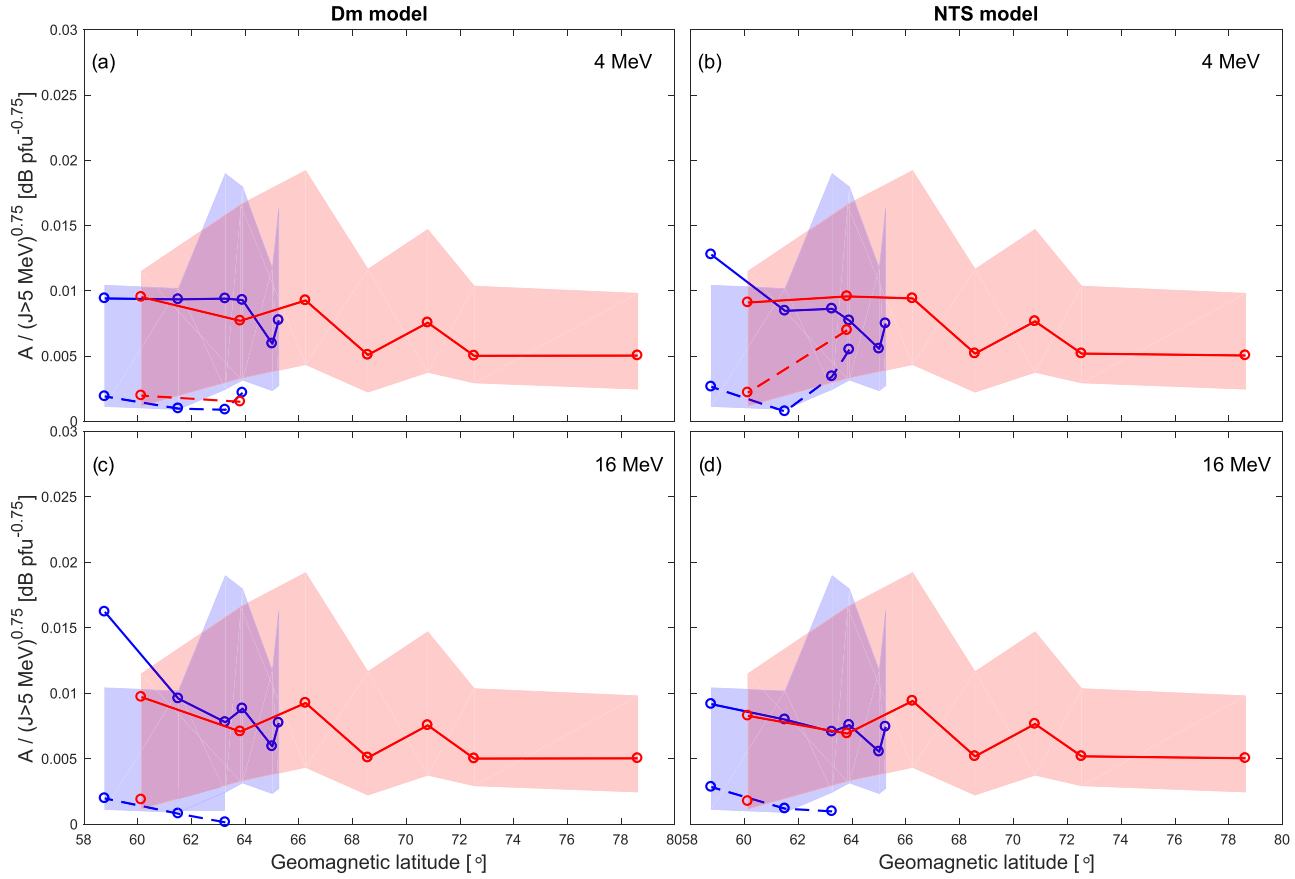

Figure 3. Median ratios of observed cosmic noise absorption and $(J(>5\,\mathrm{MeV}))^{0.75}$ as a function of geomagnetic latitude during dark conditions. Format of the figure is the same as in Figure 2.

models with 16 MeV cutoff energy (not shown) are close to the first quartile of nondivided data. The not cut A/J values for the European chain are outside the third quartile of nondivided data for most stations with all cutoff energies and both models, but are inside the 90th percentile (not shown) apart from the southernmost station (JYV, 58.92° geomagnetic latitude).

A/J values increase with decreasing geomagnetic latitude in dark conditions, possibly due to energetic electron precipitation. The spread of nondivided data is relatively larger in dark conditions than in sunlit conditions, which is understandable given the low CNA values, energetic electron precipitation from the outer radiation belt during geomagnetic storm periods (e.g., Thorne, 2010; Tian et al., 2020) induced by SPE-related coronal mass ejections, and electron precipitation from substorms (e.g., Beharrell et al., 2015; Berkey et al., 1974; Cresswell-Moorcock et al., 2013). The spread of nondivided data in dark conditions is also larger equatorward of RAN (72.59° geomagnetic latitude) than at RAN or TAL. The 8 and 32 MeV cutoff energy A/J in dark conditions from the Dm model (not shown) are very similar to those with the 16 MeV cutoff energy shown in panel (c) of Figure 3. The NTS model does not produce nightside cutoff latitudes for 8 and 32 MeV.

The A/J results from both models are quite similar for both cutoff latitude models, indicating no large systematic differences in performance between the two models. The cut A/J values with both cutoff models are close to the first quartile of the nondivided data with the higher cutoff energies indicating that the periods when the precipitating proton flux are cut are recognized by the models.

The DRAP model was used to model CNA at the riometer stations during the 73 SPEs with both cutoff models and without cutoffs. The difference between the modeled CNA and observed CNA was studied over the whole data set to evaluate the performance of the two cutoff models compared to CNA modeled without

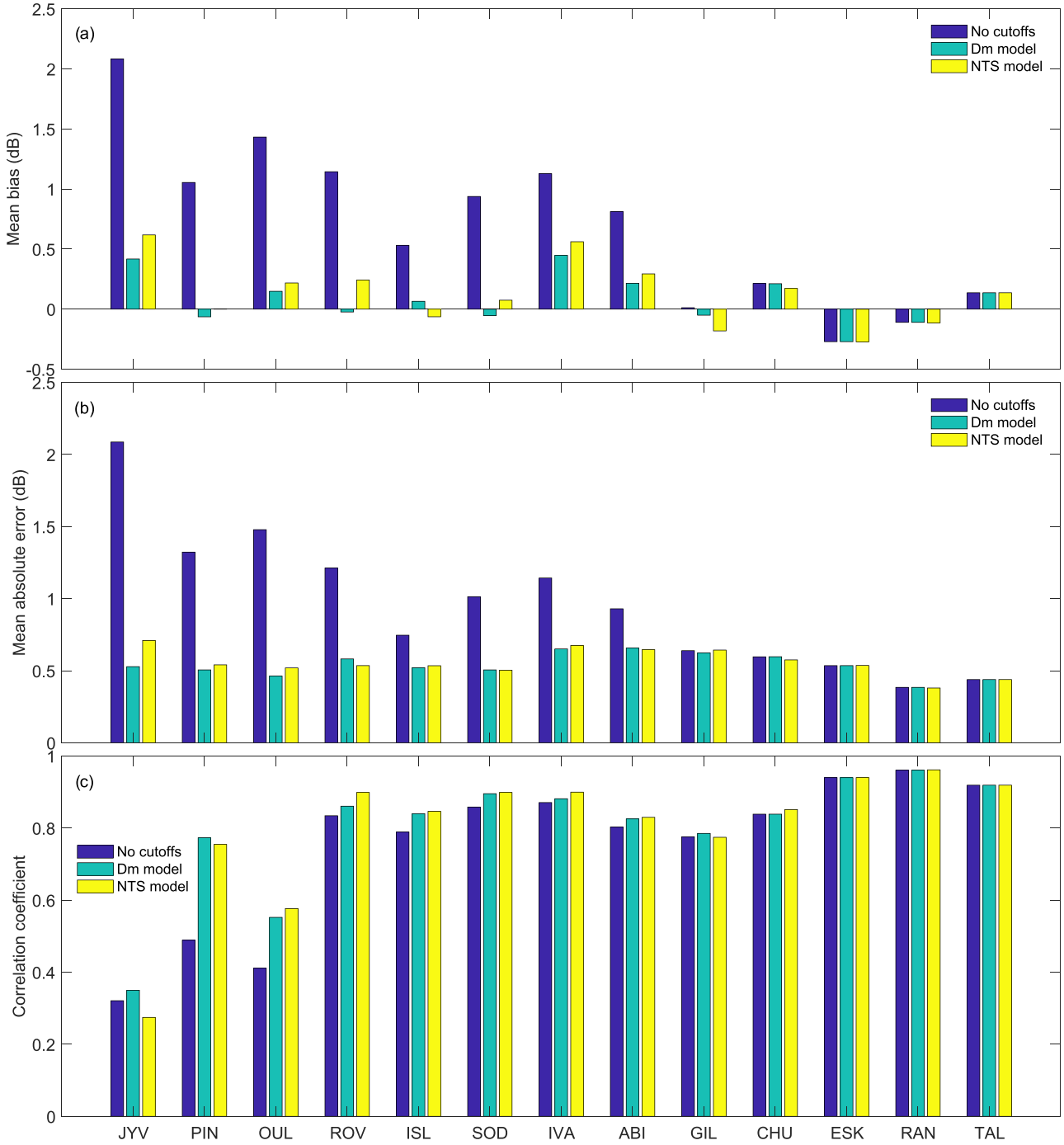

Figure 4. Statistical parameters of the difference between observations and the DRAP model at sunlit conditions without cutoffs (blue bars), DRAP with the Dm model (green bars), and DRAP with the NTS model (yellow bars) at the different riometer stations. The mean biases of the difference are shown in panel (a), the mean absolute errors of the difference are shown in panel (b), and the correlation coefficients between the model and the observations in panel (c). The stations are in ascending geomagnetic latitude order from left to right.

cutoffs and to each other. The DRAP model without cutoffs was chosen as a comparison, as this corresponds to the current implementation of uniform precipitating proton flux poleward of a fixed boundary used in climate models. The inclusion of the Dm model has been shown to improve the performance of the DRAP model compared to the standard DRAP implementation (Rogers & Honary, 2015). Therefore, if

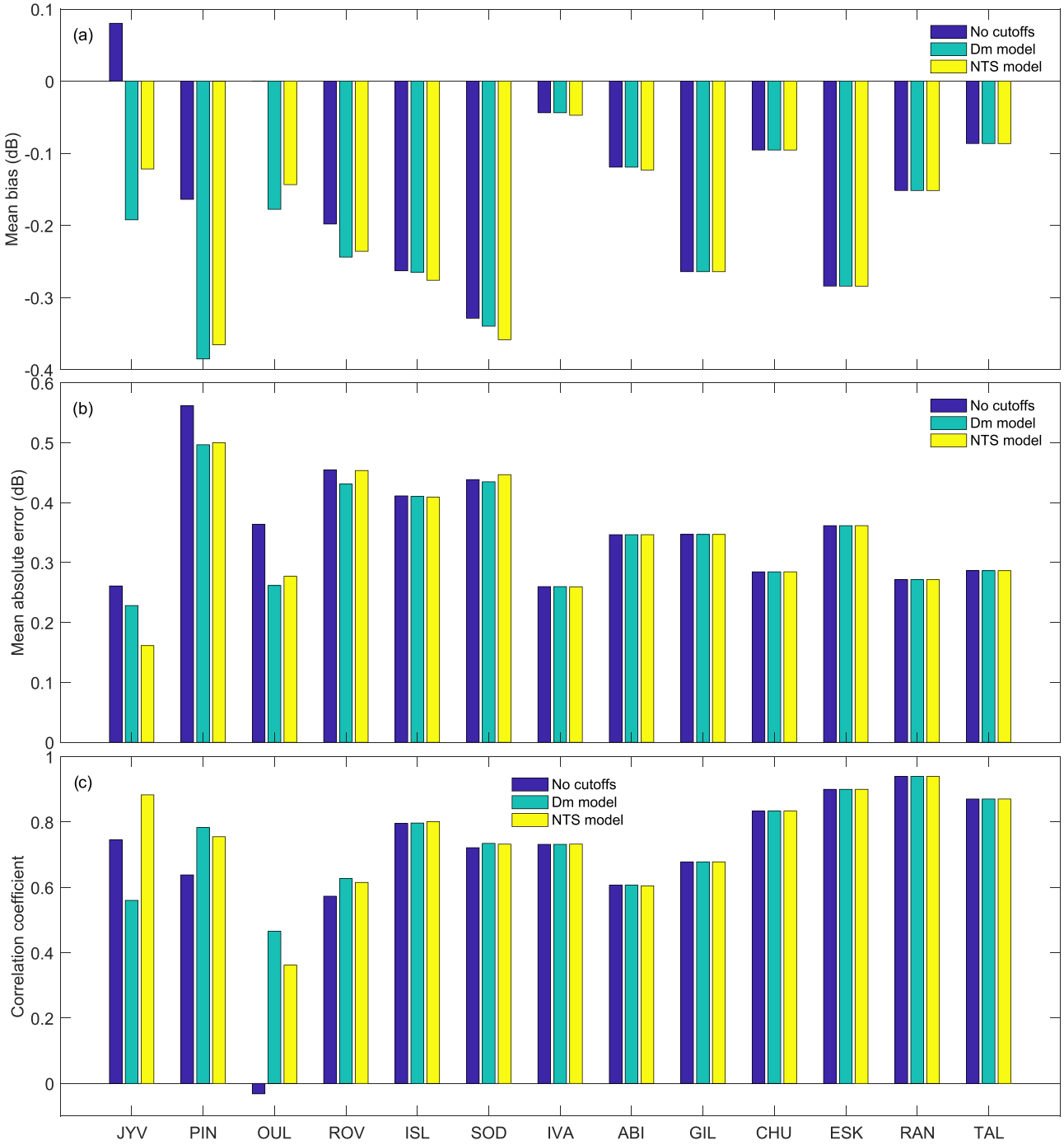

Figure 5. As in Figure 4, but for dark ionospheric conditions.

DRAP with the NTS model performs equally well or better than DRAP with the Dm model, it will also perform better than the standard version of the DRAP model. The mean biases (mean difference between modeled and observed CNA) and mean absolute errors (MAE) of the differences, and the correlations between the dayside modeled and observed CNA at the different riometer stations are shown in Figure 4. DRAP without any cutoffs is shown with blue bars, DRAP with the Dm model is shown with green bars, and DRAP with the NTS model is shown with yellow bars. The riometer stations are in ascending geomagnetic latitude order from left to right. The data were limited to times when $J(>10\,\text{MeV})$ is greater than or equal to 10 pfu and the modeled CNA without cutoffs is less than 10 dB. The upper CNA limit

was applied to reduce bias resulting from riometer nonlinearity at high CNA values (Hargreaves & Detrick, 2002; Heino et al., 2019).

The mean biases and MAEs are substantially greater, and the correlation coefficients lower, for DRAP without cutoffs than with either of the cutoff models at ABI and equatorward in sunlit conditions. The MAEs and correlation coefficients for DRAP without cutoffs and with the cutoff models are fairly similar at GIL and poleward, while the mean biases have more variation from station to station. The MAEs are fairly constant with both cutoff models across all stations, indicating consistent performance from both models. The MAEs with the NTS model are greater than with the Dm model at OUL and equatorward with the greatest difference between the two models at the most equatorward station. The mean CNA from the DRAP with the Dm model matches better with observations than from the DRAP model with the NTS model at most stations. The correlation coefficients are greater than 0.77 at and poleward of ROV for all DRAP versions. The correlation coefficients for DRAP without cutoffs drops to less than 0.5 at OUL and equatorward.

Mean biases, MAEs, and correlation coefficients were calculated for dark conditions in the same way as for the sunlit conditions and are shown in Figure 5. The mean biases for dark conditions are all negative apart from at JYV with the DRAP model without cutoffs. MAEs in dark conditions are very similar with all DRAP versions at ISL and poleward, apart from SOD, where the NTS model MAE is slightly greater than those of the two other DRAP versions. MAEs of DRAP without cutoff models are greater than with either of the cutoff models at ROV, OUL, PIN, and JYV. MAEs of the Dm model are lower than those of the NTS model at these stations, apart from JYV, where the MAE of the NTS model is significantly lower than that of the Dm model. The correlation coefficients are very similar to each other with all DRAP versions at ISL and poleward, varying between 0.60 and 0.94 from station to station. The correlation coefficients are higher with the Dm model than with the other DRAP versions at ROV, OUL, and PIN but significantly lower at JYV where the NTS model has the highest correlation coefficient. At OUL, unlike at any other station, the correlation coefficient for DRAP without cutoffs is slightly negative, but this correlation is not statistically significant based on a p-value of 0.38.

6. Discussion

The performance of both cutoff models is very similar based on the median ratios of CNA and integral proton flux showed in Figures 2 and 3. The Dm model performs better than the NTS model on the dayside based on the comparison of observed and modeled CNA shown in Figure 4, and marginally better than the NTS model on the nightside apart from the most equatorward station, JYV, where the NTS model performs better. Although the Dm model performs better than the NTS model, the differences between the two models are not very large. The Dm model is continuous in both energy and MLT, making it more straightforward to use compared to the NTS model, which produces cutoff latitudes for discrete energies and no cutoff latitudes for dusk and dawn.

Due to the form of its cutoff latitude parametrization, the Dm model can, in some cases, produce cutoff latitudes for lower energies that are equatorward of higher energy cutoff latitudes, which is not possible in reality. In addition to this, the model produces very low cutoff latitudes in highly disturbed geomagnetic conditions, when the value of the *Kp* index is high and the value of the *Dst* index low. The lowest cutoff latitudes from the Dm model in this study were in event 63 (see Table A1), where the lowest 4 MeV cutoff latitude was 37.2° invariant latitude and the lowest 32 MeV cutoff latitude was 43.5° invariant latitude. The values of the *Kp* and *Dst* indices causing the lowest cutoff latitudes were 8 and −405 nT, respectively. The most equatorward observed cutoff latitudes for SPE protons we could find in literature are about 49° invariant latitude for protons with energies of 19–27 MeV (Kress et al., 2010) and 16–35 MeV (Neal et al., 2013). Based on these extremes in cutoff latitude observations, the lowest cutoff latitudes of the Dm model seem unrealistic, especially for the lower cutoff energies used in this study. The extremely low cutoff latitudes produced by the model could possibly be corrected by adjusting the parametrization for high geomagnetic activity or by setting a fixed lower latitude boundary for the cutoff latitudes like in the NTS model. The fact that the model produces, in some cases, lower cutoff latitudes for the lower proton energies than for the higher energies needs to be taken into account when using the model in its current form. The extremely low cutoff latitudes from the Dm model could not be studied in this paper, as the locations of the riometers are limited

Table 2
Median, 10th Percentile, and 90th Percentile of the Ratio of the Area of the Dm Model Cutoff Ellipse and the Area of a Spherical Cap Limited by 60° Geomagnetic Latitude with the Different Cutoff Energies during the Studied SPEs

Energy	Median	10th percentile	90th percentile
4 MeV	0.74	0.65	1.00
8 MeV	0.77	0.69	1.02
16 MeV	0.80	0.73	1.03
32 MeV	0.85	0.78	1.06

to relatively high geomagnetic latitudes, but could be studied in the future with access to riometer data from a wider geomagnetic latitude range or by using other instruments.

The two cutoff models were studied only on the dayside and nightside with fully developed sunlit and dark ionospheres to remove the effects of twilight on CNA. Due to this approach, it is not possible to test the cutoff latitudes at dusk and dawn or the dusk-day asymmetry of the Dm model. Dawn-dusk asymmetry of low-energy proton cutoffs has been previously observed (Dmitriev et al., 2010), and in theory, the Dm model should produce a similar dawn-dusk asymmetry (cutoff latitudes more equatorward at dusk, poleward at dawn). The use of riometers also limits the possibility to validate cutoff latitudes for higher energies due to the nonlinear relationship between proton energy and CNA. CNA is mostly caused by protons with energies between about 15 to 44 MeV (Kavanagh et al., 2004; Patterson et al., 2001) in the sunlit atmosphere. These energies are consistent with the cut median ratios of CNA and integral proton flux being very close to the first quartile of the undivided data, as shown in panels (c) and (d) of Figure 2. The response of CNA to proton flux starts to drop off at higher energies and the fluxes of higher energy protons are comparatively low during SPEs. In addition to the energy-CNA-response, another limiting factor for studying higher energy cutoffs is that the locations of the riometers used in this study are limited to geomagnetic latitudes poleward of higher energy cutoff latitudes. Despite these limitations, the studied energy range and the energy-CNA-response of riometers correspond well to the altitudes of HO_x and NO_x production, and O_3 loss in the atmosphere (e.g., Turunen et al., 2009; Verronen, Seppälä, et al., 2006).

The systematically lower A/J observed by the European chain riometers compared to the Canadian chain riometers is likely due to the different methods used to determine the QDCs. The two riometer chains should observe approximately same levels of CNA with the same particle forcing and solar illumination conditions if the same QDC determination method was used for both chains, as the instruments are essentially of same design. This leaves the QDC determination method and data selection as the most likely reasons for the CNA difference between the two chains, unless some other major difference between the instruments exists that is unknown to the authors. The effect of data selection was tested by calculating new median A/J values for the Canadian chain in sunlit conditions using only events where the European chain was not affected by interference (see Table A1). This test was only done using the Dm model model to divide the data. The difference between the median A/J calculated this way and the values calculated using all available data are between -0.016 and $0.007\ \mathrm{dB\ pfu^{-1/2}}$. The absolute difference is only larger in the cut 4 MeV median A/J at GIL where the difference is $-0.023\ \mathrm{dB\ pfu^{-1/2}}$ corresponding to -15.5% of the median value calculated with all available data. Based on this, we conclude that data selection is not the reason for the significant difference between the two chains. A similar systematic difference in CNA between the two chains was also reported by Heino et al. (2019). As the analyses in this study are not comparing CNA values between the two chains, the systematic difference between the two riometer chains does not affect the results of this study. The same logic applies for the lower CNA values observed at IVA compared to the adjacent European stations and excluding or including this station does not change the overall results of the study. The effect of the two different QDC determination methods could be tested in the future by calculating new CNA values for both chains using a common QDC determination method. However, this falls outside the scope of this study.

The spatial extent of the SPE impact area compared to a static 60° geomagnetic cutoff latitude limit (e.g., Jackman et al., 2009; Matthes et al., 2017) was estimated by calculating the ratio of the area of the cutoff latitude ellipse of the Dm model on a spherical surface and the area of a spherical cap limited by 60° latitude at each time step of all SPEs used in this study. The median, and the 90th and 10th percentiles of the area ratio are shown in Table 2 for the different cutoff energies. The spatial extent of the SPE effect is significantly overestimated by the static cutoff latitude with all of the used cutoff energies. The 90th percentile of the area ratio is very close to or equal to one at all cutoff energies, indicating that the SPE impact area is underestimated by the static cutoff latitude about 10% of the time during the studied SPEs. As stated before, the Dm model produces extremely low cutoff latitudes during highly disturbed geomagnetic conditions. These extreme values

have not been removed from the distributions of the area ratio, so they skew the distributions slightly towards higher values.

GOES proton fluxes are often used as the proton precipitation input in climate models with the assumption that the full observed flux precipitates uniformly poleward of a fixed latitude boundary. Nesse Tyssøy et al. (2013) showed that geomagnetic cutoff is not present in GOES observations leading to an overestimation of energy deposition when GOES fluxes are used compared to using POES fluxes. They reported an energy deposition overestimation of 50–100% on the dayside, at and equatorward of 67° geomagnetic latitude, at 70 km altitude during the main phase of the SPE in January 2012. The total energy input overestimation at 70 km over the hemispheres was 20–30% for ≥60° geomagnetic latitude. As shown in Table 2, a static 60° geomagnetic cutoff latitude limit overestimates the SPE impact area on average by 15–25%, and underestimates it in some cases. Therefore, the implementation of a dynamic cutoff latitude model into climate model proton forcing is required for more accurate evaluation of the atmospheric effects of SPEs. A more accurate implementation of SPEs will also make it easier to validate and test forcing from other EPP sources. To our knowledge, the need for more accurate cutoff latitudes has not been reported in previous studies comparing climate models to experimental observations of the chemical effects of SPEs or in observational studies. This is likely due to the fact that the studies have focused on longer timescales, used daily or longer mean values, averaged the observations across the whole polar cap, or used observations from latitudes poleward of the cutoff latitudes (e.g., Baumgaertner et al., 2010; Funke et al., 2011; Sinnhuber et al., 2018). The need for dynamic cutoff latitudes was reported by Verronen et al. (2007) who compared hydroxyl observations from the Magnetic Limb Sounder instrument on board the Aura satellite to results from the Sodankylä Ion and Neutral Chemistry model during the January 2015 SPE (event 68, see Table A1).

Based on this study, the Dm model is a better candidate for implementation into climate models than the NTS model with the caveat that the unrealistic cutoff latitudes during times of very high geomagnetic activity are taken into account. The lower cutoff latitudes from the Dm model could also be studied with other instruments than the riometer, such as the middle latitude SuperDARN radars (Bland et al., 2018) and particle detectors on board polar orbiting satellites, to set a lower latitude limit for the cutoffs produced by the model. In the future, the Dm model could be applied with a suitable energy and time resolution to, for example, the ionization rate calculation method by Jackman (2013).

7. Conclusions

We have compared the performance of the Dmitriev et al. (2010) (Dm model) and the Nesse Tyssøy and Stadsnes (2015) (NTS model) cutoff latitude models during 73 SPEs using riometer observations and CNA modeled with the DRAP model. The cutoff latitude models were used to separate riometer observations into cut and not cut situations with multiple cutoff energies in sunlit and dark ionospheric conditions. The divided riometer data were normalized with integral proton flux observations, and the resulting ratios were studied as a function of geomagnetic latitude. Both cutoff models performed approximately equally well based on this analysis. The cutoff latitude models were also tested by implementing them into the DRAP model and comparing the resulting modeled CNA with riometer observations in sunlit and dark conditions. Based on the model comparison, the Dm model performs slightly better than the NTS model.

In addition to slightly better performance, the Dm model is continuous in cutoff energy and MLT, making it easier to implement into climate model proton forcing than the NTS model. The Dm model produces unrealistically low cutoff latitudes during periods with extreme *Kp*and *Dst* index values. Based on our results, the Dm model is more suited to use in climate models, although the unrealistic cutoff latitudes need to be taken into account when using the model.

The cutoff latitudes from the Dm model during the 73 SPEs were compared to the static 60° geomagnetic latitude cutoff limit routinely used in climate models. Based on this comparison, the single static cutoff limit overestimates the SPE impact area 90% of the time by about 15–25% with the cutoff energies used in this study. This result highlights the need for a more realistic proton precipitation implementation in climate and chemistry models in the future.

Appendix A: List of Studied Solar Proton Events

Table A1
Solar Proton Events Used in This Study

Event	SPE start time (UT)	Max >10 MeV flux (pfu)	Event	SPE start time (UT)	Max >10 MeV flux (pfu)
1	04 Nov 1997 08:30	72	38[a]	19 Nov 2001 12:30	34
2	06 Nov 1997 13:05	490	39[a]	22 Nov 2001 23:20	18,900
3	24 Aug 1998 23:55	670	40[a]	26 Dec 2001 06:05	779
4	25 Sep 1998 00:10	44	41[a]	29 Dec 2001 05:10	76
5	30 Sep 1998 15:20	1,200	42[a]	30 Dec 2001 02:45	108
6	08 Nov 1998 02:45	11	43[a]	10 Jan 2002 20:45	91
7	23 Jan 1999 11:05	14	44[a]	15 Jan 2002 14:35	15
8	05 May 1999 18:20	14	45[a]	20 Feb 2002 07:30	13
9	02 Jun 1999 02:45	48	46[a]	17 Mar 2002 08:20	13
10[a]	18 Feb 2000 11:30	13	47[a]	18 Mar 2002 13:00	53
11	04 Apr 2000 20:55	55	48[a]	20 Mar 2002 15:10	19
12	07 Jun 2000 13:35	55	49[a]	22 Mar 2002 20:20	16
13	10 Jun 2000 18:05	46	50	17 Apr 2002 15:30	24
14	14 Jul 2000 10:45	24,000	51	21 Apr 2002 02:25	2,520
15	22 Jul 2000 13:20	17	52	22 May 2002 17:55	820
16	28 Jul 2000 10:50	18	53	07 Jul 2002 18:30	22
17	11 Aug 2000 16:50	17	54	16 Jul 2002 17:50	234
18	12 Sep 2000 15:55	320	55	19 Jul 2002 10:50	13
19[a]	16 Oct 2000 11:25	15	56	22 Jul 2002 06:55	28
20[a]	26 Oct 2000 00:40	15	57	14 Aug 2002 09:00	26
21[a]	08 Nov 2000 23:50	14,800	58	22 Aug 2002 04:40	36
22[a]	24 Nov 2000 15:20	942	59	24 Aug 2002 01:40	317
23[a]	28 Jan 2001 20:25	49	60	07 Sep 2002 04:40	208
24[a]	29 Mar 2001 16:35	35	61	09 Nov 2002 19:20	404
25[a]	02 Apr 2001 23:40	1,110	62	04 Nov 2003 22:25	353
26[a]	10 Apr 2001 08:50	355	63[a]	21 Nov 2003 23:55	13
27[a]	15 Apr 2001 14:10	951	64[a]	02 Dec 2003 15:05	86
28[a]	18 Apr 2001 03:15	321	65	25 Jul 2004 18:55	2,086
29[a]	28 Apr 2001 04:30	57	66	01 Nov 2004 06:55	63
30	07 May 2001 19:15	30	67	07 Nov 2004 19:10	495
31	15 Jun 2001 17:50	26	68	16 Jan 2005 02:10	5,040
32	10 Aug 2001 10:20	17	69	14 May 2005 05:25	3,140
33	16 Aug 2001 01:35	493	70	14 Jul 2005 02:45	134
34	24 Sep 2001 12:15	12,900	71	27 Jul 2005 23:00	41
35	01 Oct 2001 11:45	2,360	72	22 Aug 2005 20:40	330
36[a]	19 Oct 2001 22:25	11	73	14 Aug 2010 12:30	14
37[a]	04 Nov 2001 17:05	31,700			

[a]SGO stations affected by unknown radio interference.

Data Availability Statement

The Sodankylä Geophysical Observatory riometer chain data was provided by Antti Kero from University of Oulu/Sodankylä Geophysical Observatory (Finland). The GO-Canada riometer array is operated by the University of Calgary with financial support from the Canadian Space Agency. All GO-Canada riometer data is openly available from data.phys.ucalgary.ca. NOAA GOES particle flux data are openly available online from https://www.ngdc.noaa.gov/stp/satellite/goes/dataaccess.html. *Kp* and *Dst* index data are available from the World Data Center (WDC) for Geomagnetism, Kyoto at https://wdc.kugi.kyoto-u.ac.jp/wdc/Sec3.html. Solar wind data are available through National Aeronautics and Space Administration's OMNIWeb service at https://omniweb.gsfc.nasa.gov/.

Acknowledgments
The work of EH was supported by the Research Council of Norway under contract 287427 and the work of NP was supported by the Research Council of Norway under CoE contract 223252. The authors would also like to acknowledge the openly available jLab data analysis package for Matlab (Lilly, 2017), which was used for parts of the plotting in this paper.

References

Akmaev, R. A. (2010). D-RAP Model Validation: I. Scientific Report. Retrieved from https://www.ngdc.noaa.gov/stp/drap/DRAP-V-Report1.pdf

Andersson, M. E., Verronen, P. T., Rodger, C. J., Clilverd, M. A., & Seppälä, A. (2014). Missing driver in the Sun–Earth connection from energetic electron precipitation impacts mesospheric ozone. *Nature Communications*, *5*, 5197. https://doi.org/10.1038/ncomms6197

Baumgaertner, A. J. G., Jöckel, P., Riede, H., Stiller, G., & Funke, B. (2010). Energetic particle precipitation in ECHAM5/MESSy—Part 2: Solar proton events. *Atmospheric Chemistry and Physics*, *10*(15), 7,285–7,302. https://doi.org/10.5194/acp-10-7285-2010

Baumgaertner, A. J. G., Seppälä, A., Jöckel, P., & Clilverd, M. A. (2011). Geomagnetic activity related NO_x enhancements and polar surface air temperature variability in a chemistry climate model: Modulation of the NAM index. *Atmospheric Chemistry and Physics*, *11*(9), 4,521–4,531. https://doi.org/10.5194/acp-11-4521-2011

Beharrell, M. J., Honary, F., Rodger, C. J., & Clilverd, M. A. (2015). Substorm-induced energetic electron precipitation: Morphology and prediction. *Journal of Geophysical Research: Space Physics*, *120*, 2,993–3,008. https://doi.org/10.1002/2014JA020632

Berkey, F., Driatskiy, V., Henriksen, K., Hultqvist, B., Jelly, D., Shchuka, T., et al. (1974). A synoptic investigation of particle precipitation dynamics for 60 substorms in IQSY (1964–1965) and IASY (1969). *Planetary and Space Science*, *22*(2), 255–307. https://doi.org/10.1016/0032-0633(74)90028-2

Birch, M. J., Hargreaves, J. K., Senior, A., & Bromage, B. J. I. (2005). Variations in cutoff latitude during selected solar energetic proton events. *Journal of Geophysical Research: Space Physics*, *110*, A07221. https://doi.org/10.1029/2004JA010833

Blake, J., McNab, M., & Mazur, J. (2001). Solar-proton polar-cap intensity structures as a test of magnetic field models. *Advances in Space Research*, *28*(12), 1,753–1,757. https://doi.org/10.1016/S0273-1177(01)00542-7

Bland, E. C., Heino, E., Kosch, M. J., & Partamies, N. (2018). SuperDARN radar-derived HF radio attenuation during the September 2017 solar proton events. *Space Weather*, *16*, 1455–1469. https://doi.org/10.1029/2018SW001916

Clilverd, M. A., Rodger, C. J., Moffat-Griffin, T., & Verronen, P. T. (2007). Improved dynamic geomagnetic rigidity cutoff modeling: Testing predictive accuracy. *Journal of Geophysical Research*, *112*, A08302. https://doi.org/10.1029/2007JA012410

Cresswell-Moorcock, K., Rodger, C. J., Kero, A., Collier, A. B., Clilverd, M. A., Häggström, I., & Pitkänen, T. (2013). A reexamination of latitudinal limits of substorm-produced energetic electron precipitation. *Journal of Geophysical Research: Space Physics*, *118*, 6,694–6,705. https://doi.org/10.1002/jgra.50598

Dmitriev, A. V., Jayachandran, P. T., & Tsai, L.-C. (2010). Elliptical model of cutoff boundaries for the solar energetic particles measured by POES satellites in December 2006. *Journal of Geophysical Research*, *115*, A12244. https://doi.org/10.1029/2010JA015380

Fanselow, J. L., & Stone, E. C. (1972). Geomagnetic cutoffs for cosmic-ray protons for seven energy intervals between 1.2 and 39 MeV. *Journal of Geophysical Research*, *77*(22), 3,999–4,009. https://doi.org/10.1029/JA077i022p03999

Funke, B., Baumgaertner, A., Calisto, M., Egorova, T., Jackman, C. H., Kieser, J., et al. (2011). Composition changes after the "Halloween" solar proton event: The High Energy Particle Precipitation in the Atmosphere (HEPPA) model versus MIPAS data intercomparison study. *Atmospheric Chemistry and Physics*, *11*(17), 9,089–9,139. https://doi.org/10.5194/acp-11-9089-2011

Gillett, N. P., & Thompson, D. W. J. (2003). Simulation of recent Southern Hemisphere climate change. *Science*, *302*(5643), 273–275. https://doi.org/10.1126/science.1087440

Gray, L. J., Beer, J., Geller, M., Haigh, J. D., Lockwood, M., Matthes, K., et al. (2010). Solar influences on the climate. *Reviews of Geophysics*, *48*, RG4001. https://doi.org/10.1029/2009RG000282

Hargreaves, J. K., & Detrick, D. L. (2002). Application of polar cap absorption events to the calibration of riometer systems. *Radio Science*, *37*(3), 1035. https://doi.org/10.1029/2001RS002465

Heino, E., Verronen, P. T., Kero, A., Kalakoski, N., & Partamies, N. (2019). Cosmic noise absorption during solar proton events in WACCM-D and riometer observations. *Journal of Geophysical Research: Space Physics*, *124*, 1,361–1,376. https://doi.org/10.1029/2018JA026192

Jackman, C. H. (2013). Ionization rates for 1963–2012 from solar proton events. Retrieved from https://solarisheppa.geomar.de/solar-isheppa/sites/default/files/data/SOLARIS_Jackman_SPEs.pdf

Jackman, C. H., Marsh, D. R., Vitt, F. M., Garcia, R. R., Randall, C. E., Fleming, E. L., & Frith, S. M. (2009). Long-term middle atmospheric influence of very large solar proton events. *Journal of Geophysical Research*, *114*, D11304. https://doi.org/10.1029/2008JD011415

Kallenrode, M.-B. (2003). Current views on impulsive and gradual solar energetic particle events. *Journal of Physics G: Nuclear Physics*, *29*, 965–981. https://doi.org/10.1088/0954-3899/29/5/316

Kavanagh, A., Marple, S., Honary, F., McCrea, I., & Senior, A. (2004). On solar protons and polar cap absorption: Constraints on an empirical relationship. *Annales Geophysicae*, *22*, 1,133–1,147. https://doi.org/10.5194/angeo-22-1133-2004

Kress, B. T., Mertens, C. J., & Wiltberger, M. (2010). Solar energetic particle cutoff variations during the 29–31 October 2003 geomagnetic storm. *Space Weather*, *8*, 5. https://doi.org/10.1029/2009SW000488

Leske, R. A., Mewaldt, R. A., Stone, E. C., & von Rosenvinge, T. T. (2001). Observations of geomagnetic cutoff variations during solar energetic particle events and implications for the radiation environment at the space station. *Journal of Geophysical Research*, *106*(A12), 30,011–30,022. https://doi.org/10.1029/2000JA000212

Lilly, J. M. (2017). jLab: A data analysis package for Matlab, v. 1.6.5. Retrieved from http://www.jmlilly.net/jmlsoft.html

Little, C. G., & Leinbach, H. (1958). Some measurements of high-latitude ionospheric absorption using extraterrestrial radio waves. *Proceedings of the IRE*, *46*(1), 334–348. https://doi.org/10.1109/JRPROC.1958.286795

Little, C. G., & Leinbach, H. (1959). The Riometer—A device for the continuous measurement of ionospheric absorption. *Proceedings of the IRE*, *47*(2), 315–320. https://doi.org/10.1109/JRPROC.1959.287299

Matthes, K., Funke, B., Andersson, M. E., Barnard, L., Beer, J., Charbonneau, P., et al. (2017). Solar forcing for CMIP6 (v3.2). *Geoscientific Model Development*, *10*(6), 2,247–2,302. https://doi.org/10.5194/gmd-10-2247-2017

Neal, J. J., Rodger, C. J., & Green, J. C. (2013). Empirical determination of solar proton access to the atmosphere: Impact on polar flight paths. *Space Weather*, *11*, 420–433. https://doi.org/10.1002/swe.20066

Nesse Tyssøy, H., & Stadsnes, J. (2015). Cutoff latitude variation during solar proton events: Causes and consequences. *Journal of Geophysical Research: Space Physics*, *120*, 553–563. https://doi.org/10.1002/2014JA020508

Nesse Tyssøy, H., Stadsnes, J., Søraas, F., & Sørbø, M. (2013). Variations in cutoff latitude during the January 2012 solar proton event and implication for the distribution of particle energy deposition. *Geophysical Research Letters*, *40*, 4,149–4,153. https://doi.org/10.1002/grl.50815

Ogliore, R. C., Mewaldt, R. A., Leske, R. A., Stone, E. C., & von Rosenvinge, T. T. (2001). A direct measurement of the geomagnetic cutoff for cosmic rays at space station latitudes. *International Cosmic Ray Conference*, *10*, 4,112.

Patterson, J. D., Armstrong, T. P., Laird, C. M., Detrick, D. L., & Weatherwax, A. T. (2001). Correlation of solar energetic protons and polar cap absorption. *Journal of Geophysical Research*, *106*(A1), 149–163. https://doi.org/10.1029/2000JA002006

Potemra, T. A. (1972). The empirical connection of riometer absorption to solar protons during PCA events. *Radio Science*, *7*(5), 571–577. https://doi.org/10.1029/RS007i005p00571

Reames, D. V. (1999). Particle acceleration at the Sun and in the heliosphere. *Space Science Reviews*, *90*(3), 413–491. https://doi.org/10.1023/A:1005105831781

Rodger, C. J., Clilverd, M. A., Verronen, P. T., Ulich, T., Jarvis, M. J., & Turunen, E. (2006). Dynamic geomagnetic rigidity cutoff variations during a solar proton event. *Journal of Geophysical Research*, *111*, A04222. https://doi.org/10.1029/2005JA011395

Rogers, N. C., & Honary, F. (2015). Assimilation of real-time riometer measurements into models of 30 MHz polar cap absorption. *Journal of Space Weather and Space Climate*, *5*(27), A8. https://doi.org/10.1051/swsc/2015009

Rogers, N. C., Kero, A., Honary, F., Verronen, P. T., Warrington, E. M., & Danskin, D. W. (2016). Improving the twilight model for polar cap absorption nowcasts. *Space Weather*, *14*, 950–972. https://doi.org/10.1002/2016SW001527

Rostoker, G., Samson, J. C., Creutzberg, F., Hughes, T. J., McDiarmid, D. R., McNamara, A. G., et al. (1995). CANOPUS—A ground-based instrument array for remote sensing the high latitude ionosphere during the ISTP/GGS program. *Space Science Reviews*, *71*(1), 743–760. https://doi.org/10.1007/BF00751349

Sauer, H. H., & Wilkinson, D. C. (2008). Global mapping of ionospheric HF/VHF radio wave absorption due to solar energetic protons. *Space Weather*, *6*, S12002. https://doi.org/10.1029/2008SW000399

Sellers, B., Hanser, F. A., Stroscio, M. A., & Yates, G. K. (1977). The night and day relationships between polar cap riometer absorption and solar protons. *Radio Science*, *12*(5), 779–789. https://doi.org/10.1029/RS012i005p00779

Seppälä, A., Randall, C. E., Clilverd, M. A., Rozanov, E., & Rodger, C. J. (2009). Geomagnetic activity and polar surface air temperature variability. *Journal of Geophysical Research*, *114*, A10312. https://doi.org/10.1029/2008JA014029

Sinnhuber, M., Berger, U., Funke, B., Nieder, H., Reddmann, T., Stiller, G., et al. (2018). NO_y production, ozone loss and changes in net radiative heating due to energetic particle precipitation in 2002–2010. *Atmospheric Chemistry and Physics*, *18*(2), 1,115–1,147. https://doi.org/10.5194/acp-18-1115-2018

Sinnhuber, M., Nieder, H., & Wieters, N. (2012). Energetic particle precipitation and the chemistry of the mesosphere/lower thermosphere. *Surveys in Geophysics*, *33*(6), 1,281–1,334. https://doi.org/10.1007/s10712-012-9201-3

Smart, D. (1999). Changes in calculated vertical cutoff rigidities at the altitude of the International Space Station as a function of geomagnetic activity. *Proceedings of the 26th International Cosmic Ray Conference*, *7*, 337.

Smart, D., & Shea, M. (2001). A comparison of the Tsyganenko model predicted and measured geomagnetic cutoff latitudes. *Advances in Space Research*, *28*(12), 1,733–1,738. https://doi.org/10.1016/S0273-1177(01)00539-7

Smart, D., & Shea, M. (2003). The space-developed dynamic vertical cutoff rigidity model and its applicability to aircraft radiation dose. *Advances in Space Research*, *32*(1), 103–108. https://doi.org/10.1016/S0273-1177(03)90376-0

Smart, D., & Shea, M. (2009). Fifty years of progress in geomagnetic cutoff rigidity determinations. *Advances in Space Research*, *44*(10), 1107–1123. https://doi.org/10.1016/j.asr.2009.07.005

Stauning, P. (1996). Investigations of ionospheric radio wave absorption processes using imaging riometer techniques. *Journal of Atmospheric and Terrestrial Physics*, *58*, 753–764. https://doi.org/10.1016/0021-9169(95)00072-0

Størmer, C. (1955). *The polar aurora*. Oxford: Clarendon Press.

Thorne, R. M. (2010). Radiation belt dynamics: The importance of wave-particle interactions. *Geophysical Research Letters*, *37*, L22107. https://doi.org/10.1029/2010GL044990

Tian, X., Yu, Y., & Yue, C. (2020). Statistical survey of storm-time energetic particle precipitation. *Journal of Atmospheric and Solar-Terrestrial Physics*, *199*, 105,204. https://doi.org/10.1016/j.jastp.2020.105204

Turunen, E., Verronen, P. T., Seppälä, A., Rodger, C. J., Clilverd, M. A., Tamminen, J., et al. (2009). Impact of different energies of precipitating particles on NO_x generation in the middle and upper atmosphere during geomagnetic storms. *Journal of Atmospheric and Solar-Terrestrial Physics*, *71*(10), 1,176–1,189. https://doi.org/10.1016/j.jastp.2008.07.005

Vainio, R., Desorgher, L., Heynderickx, D., Storini, M., Flückiger, E., Horne, R. B., et al. (2009). Dynamics of the Earth's particle radiation environment. *Space Science Reviews*, *147*(3), 187–231. https://doi.org/10.1007/s11214-009-9496-7

Verronen, P. T., Rodger, C. J., Clilverd, M. A., Pickett, H. M., & Turunen, E. (2007). Latitudinal extent of the January 2005 solar proton event in the Northern Hemisphere from satellite observations of hydroxyl. *Annales Geophysicae*, *25*(10), 2203–2215. https://doi.org/10.5194/angeo-25-2203-2007

Verronen, P. T., Seppälä, A., Kyrölä, E., Tamminen, J., Pickett, H. M., & Turunen, E. (2006). Production of odd hydrogen in the mesosphere during the January 2005 solar proton event. *Geophysical Research Letters*, *33*, L24811. https://doi.org/10.1029/2006GL028115

Verronen, P. T., Ulich, T., Turunen, E., & Rodger, C. J. (2006). Sunset transition of negative charge in the D-region ionosphere during high-ionization conditions. *Annales Geophysicae*, *24*(1), 187–202. https://doi.org/10.5194/angeo-24-187-2006